J Mater Sci: Mater Electron (2016) 27:11017–11033
DOI 10.1007/s10854-016-5218-6

Photo-degradation of Congored, acid brown and acid violet: photo catalyst and magnetic investigation of $CuFe_2O_4$–TiO_2–Ag nanocomposites

Shamin Masoumi[1] · Gholamreza Nabiyouni[1] · Davood Ghanbari[2]

Received: 17 May 2016 / Accepted: 17 June 2016 / Published online: 22 June 2016
© Springer Science+Business Media New York 2016

Abstract Copper ferrite ($CuFe_2O_4$) nanoparticles were first synthesized via a microwave-assisted method. Then $CuFe_2O_4$–TiO_2 nanocomposites were prepared using sol–gel method. The silver nanoparticles were produced through reduction of silver nitrate ($AgNO_3$) with sodium borohydride ($NaBH_4$). By addition $NaBH_4$–$AgNO_3$ in the presence of the $CuFe_2O_4$–TiO_2, nanocomposite of $CuFe_2O_4$–TiO_2–Ag was produced by a simple precipitation method. This nanocomposite was also prepared using hydrothermal method. The prepared products were characterized by X-ray diffraction, scanning electron microscopy, and Fourier transform infrared spectroscopy. Alternating gradient force magnetometer was used to study the magnetic property of the products. The results illustrated superparamagnetic behaviour of $CuFe_2O_4$ nanoparticles. The photo-catalytic behaviour of $CuFe_2O_4$–TiO_2–Ag nanocomposites was evaluated using the degradation of three various azo dyes under ultraviolet light and visible light irradiation. These results suggest that the prepared nanocomposites are applicable for magnetic and photocatalytic performance in both visible and UV light.

✉ Gholamreza Nabiyouni
G-nabiyouni@araku.ac.ir

[1] Department of Physics, Faculty of Science, Arak University, Arāk 38156-88349, Iran

[2] Young Researchers and Elite Club, Arak Branch, Islamic Azad University, Arāk, Iran

1 Introduction

Photocatalytic technology provides a facile and cheap method for eliminate inorganic and organic pollutants from wastewater, since most pollutants could be degraded or mineralized by use of photocatalytic degradation technology. A number of well known semiconductors, such as TiO_2, ZnO, Bi_2O_3, WO_3, V_2O_5, SnO_2, Fe_2O_3, CdS, have been studied as photocatalysts. Successful examples of cocatalysts include cases where overall water splitting has been achieved by dispersing metal or metal oxide nanoparticles on the surface of photocatalyst particles [1–3]. Metal oxide photocatalytic degradation of organic pollutants has attracted significant attention by researchers because of its usefulness in tackling environmental contaminants. Whereas TiO_2 as a metal oxide seems to be one of the most promising semiconductors for many photocatalytic applications due to its low cost, chemical stability, nontoxicity, water insolubility, hydrophilicity, itsavailability and non-toxicity. Its utilization remains typically confined to UV light because of its wide band gap (3.2 eV for anatase and 3.0 eV for rutile). TiO_2 has been investigated extensively for optical, electrical, and photochemical applications, due to its chemical stability and good performance. In the recent years, one-dimensional TiO_2 has enormous potential as photocatalysts, solar cells, nanodevices and sensors because of their peculiar properties, which originate from their low dimensionality [4, 5]. TiO_2 is a widely used and studied photocatalyst due to its remarkable ability to harness the energy of photons to drive oxidation/reduction reactions. In addition to being photochemically active, TiO_2 is inexpensive and generally stable in solution, and its band edges straddle the reduction–oxidation potentials of many valuable chemical processes [6]. However, the TiO_2 photocatalyst still cannot be

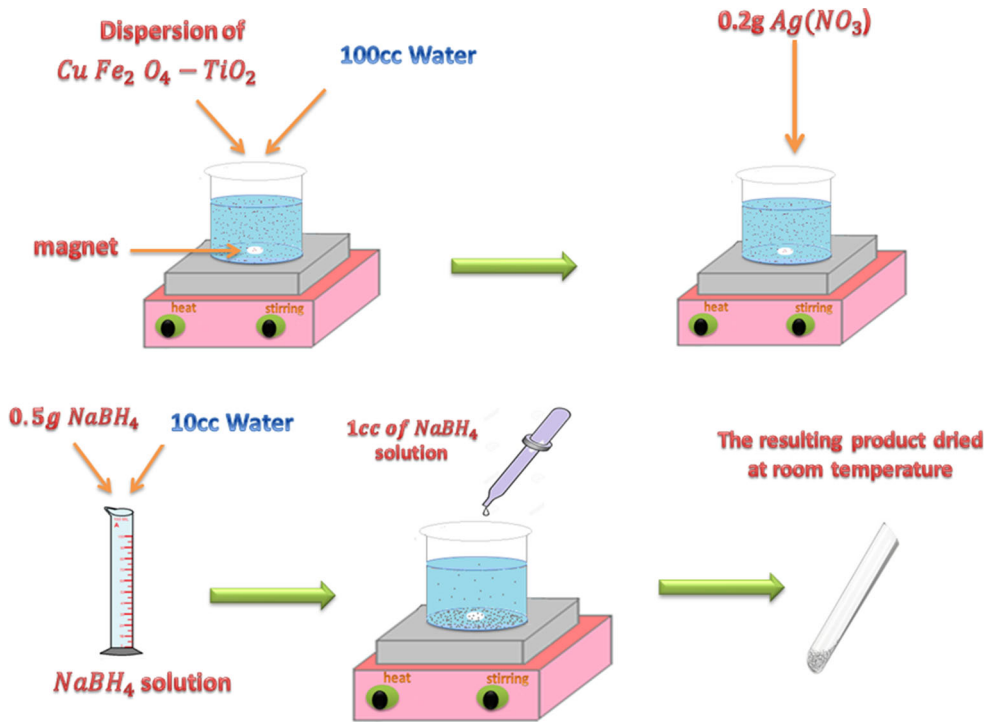

Fig. 1 Schematic of nanocomposite preparation

widely used in practical applications due to its limited visible-light absorption and low photocatalytic yield. Recently, it was discovered that plasmonic noble metal nanoparticles, such as Au and Ag, are capable of sensitizing wide-bandgap semiconductors for example titanium dioxide (TiO_2), exhibiting much enhanced visible-light response [7]. Nanoparticles of noble metals (such as Ag, Au, Pt, etc.) can strongly absorb visible light due to their localized surface plasmon resonance (LSPR), which can be tuned by varying their size, surrounding and shape. When the frequency of the event light satisfies the resonance conditions of the noble-metal NPs, the LSPR occurs with the associated light absorption. Moreover, noble metal NPs can also work as an electron trap and active reaction sites [8, 9]. Plasmon resonant nanostructures have gained remarkable interest in many fields, medicine, including near-field optics, surface enhanced spectroscopy, and solar cells. More recently, researchers have explored the applicability of plasmonic processes in the field of photocatalytic chemistry for organic molecule decomposition CO oxidation, and even materials synthesis. Various enhancement mechanisms have been proposed, comprising plasmonic heating and charge transfer [10]. Over the last two decades, noble metal nanoparticles (NPs) have been the subject of extensive research in the frame of nanotechnology, mainly owing to their unique optical properties. Indeed, the free electron gas of such NPs features a resonant oscillation upon illumination in the visible part of the spectrum. The spectral properties of this resonance depend on the constitutive material, the geometry of the NP and its environment. This resonant electronic oscillation is called localized surface plasmon (LSP), and the field of research that studies the fundamentals and applications of LSP is known as nanoplasmonics. LSPs are accompanied by valuable physical effects such as optical near-field enhancement, heat generation and excitation of hot-electrons. Hence, plasmonic NPs can behave as efficient nanosources of heat, light or energetic electrons, remotely controllable by light [11]. The composites of semiconductor nanoparticles and optically active metallic nanostructures represent a promising alternative to conventional photocatalysts. The main feature of these photocatalysts is that the interaction between semiconductor and metallic building blocks results in very efficient conversion of incident photons into electron–hole pairs in the semiconductor [12]. These factors gave rise to a new approach to efficient visible light photocatalysts, namely, depositing the noble metal NPs on the surface of a suitable polar semiconductor such as TiO_2 to form a metal–semiconductor composite photocatalyst. The plasmonic effect exerted by the different metallic particles critically influences degradation of organic compounds in liquids under both ultraviolet (UV) and visible-light irradiations. Recently, the plasmonic effect is exploited to extend the photocatalytic activity of composites into visible light region. Under the visible light irradiation, the electrons generated on the Ag nanoparticles based on the Plasmon excitation can transfer to the neighboring TiO_2 particles which function as the

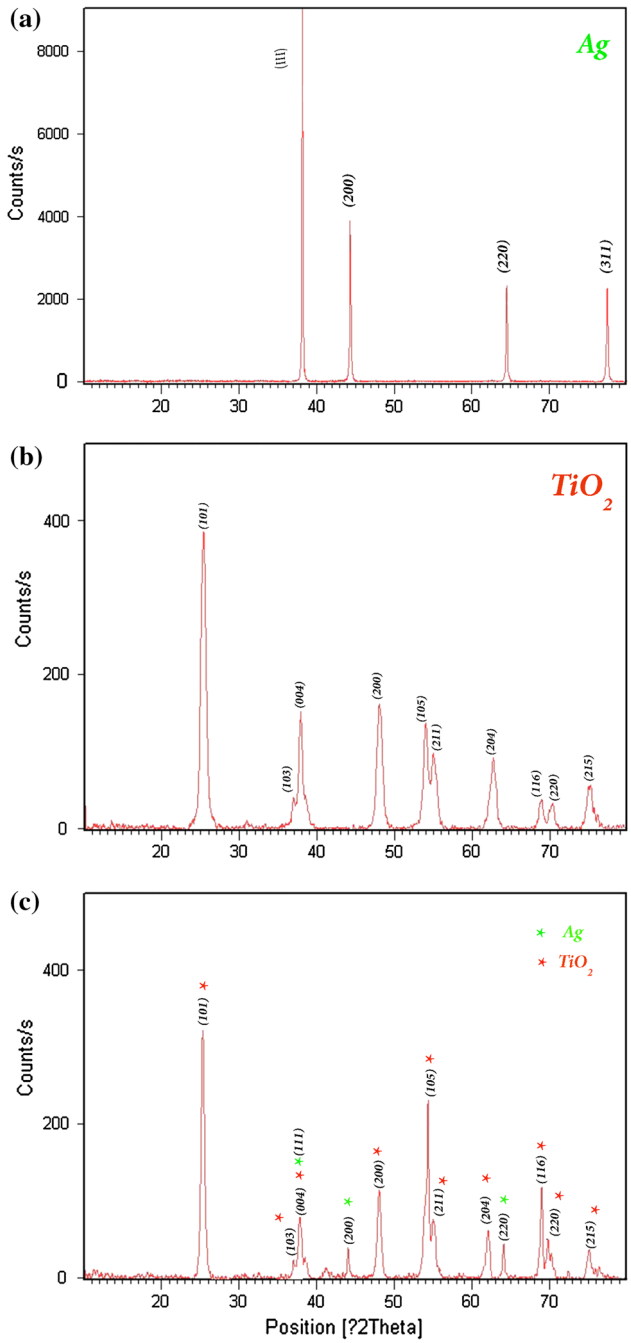

Fig. 2 XRD pattern of **a** silver nanoparticle, **b** TiO_2 nanoparticles, **c** TiO_2–Ag nanocomposite

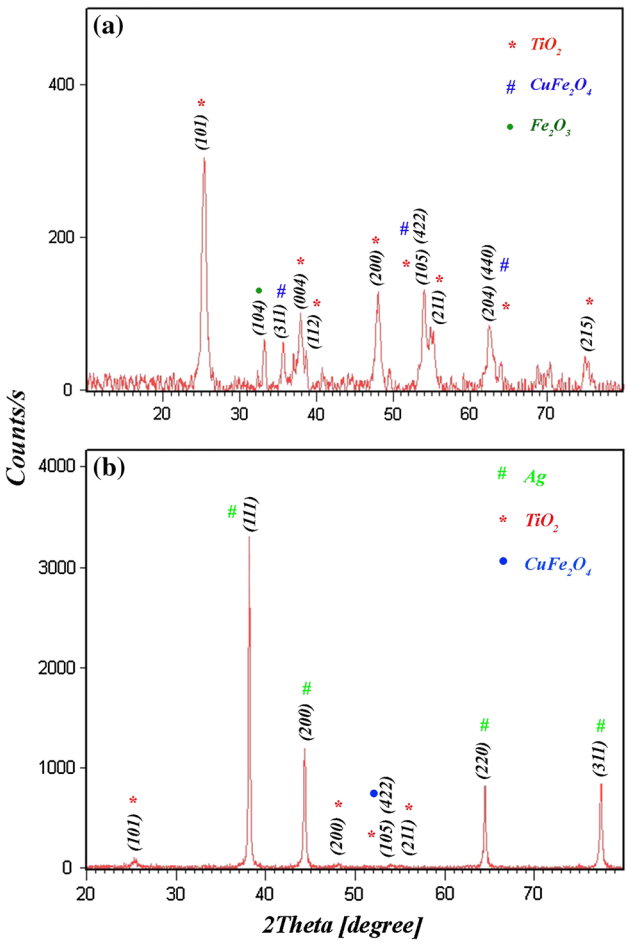

Fig. 3 XRD pattern of **a** $CuFe_2O_4$–TiO_2 nanocomposite, **b** $CuFe_2O_4$–TiO_2–Ag nanocomposite by precipitation method

photocatalytic centers [13, 14]. The surface loading of metallic Ag nanoparticles on various semiconductors has been demonstrated to be an effective method for the improved photocatalytic performance. It is generally accepted that metallic Ag nanoparticle functions as an electron sink to accept photogenerated electrons from excited semiconductor facilitating O_2 reduction [15]. One of the alternative approaches for achieving the threshold of the photo-response of titanium dioxide into the visible region is to make a composite semiconductor by modifying TiO_2 with noble metals. Recent results demonstrate the execution of photocatalysis on coinage (Ag, Au and Cu) metal nanoparticles through the excitation of localized surface plasmon resonance (LSPR) [16]. The use of LSPR excitation to drive photocatalysis falls primarily into two categories: (a) direct photocatalysis, where coinage metal nanoparticles act as the light absorber and the catalytically active site and (b) indirect photocatalysis, where excitation of LSPR is used to transfer photon energy to nearby semiconductors. In particular, silver as a noble metal has attracted remarkable attention, as a result of its considerable role in the improvement of the photo-activity of semiconductors [17]. Synthesis of TiO_2-based composites via the incorporation of noble metal nanoparticles is known to enhance the photocatalytic performance, since noble metals can lock the photogenerated electrons. Subsequently, the electron transfer rate at the interface increases, which leads to an increase in the photocatalytic activity of

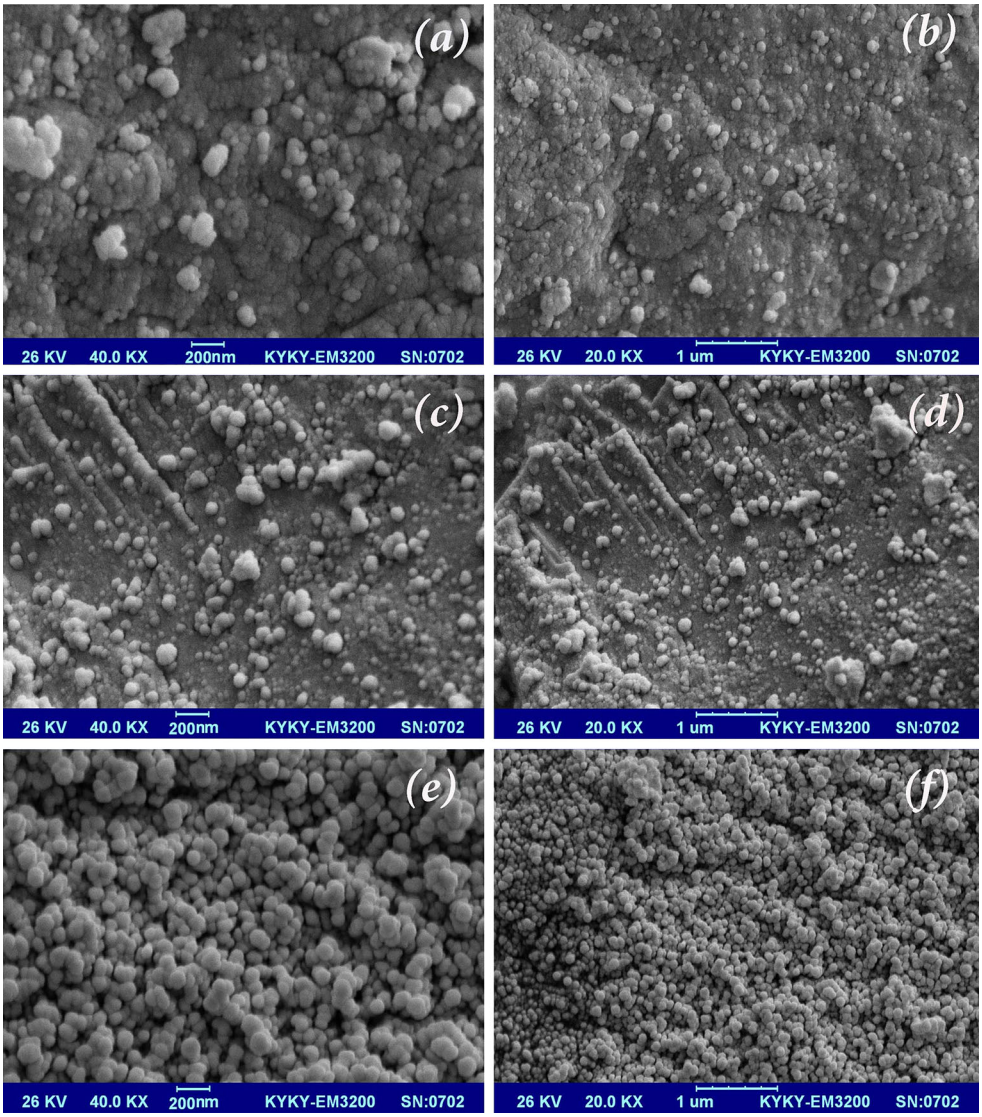

Fig. 4 SEM images of $CuFe_2O_4$ **a**, **b** 170 W, **c**, **d** 680 W, **e**, **f** 850 W

TiO_2 [18]. One of the common methods to retard the recombination and to enhance the charge separation efficiency (hence the photocatalytic activity) is to load noble metal nanoparticles on the surface of photocatalysts, which forms Schottky junction at the semiconductor/metal interface [19]. The striking feature of silver nanocomposites combined with magnetic nanoparticles is that they can be readily separated using an external magnet, providing a simple separation of the nanocomposite. Finally, by using these materials for killing bacteria under a magnetic field, we can expect a short sample preparation time and an easy clean up procedure [20]. Nanocrystalline ferrites with the general formula of MFe_2O_4 (M = Mn, Co, Ni, Cu, or Zn) are very important magnetic materials because of their interesting magnetic and electrical properties with chemical and thermal stabilities. Copper ferrite ($CuFe_2O_4$) is one of the most important ferrites. By the prominent goodness of magnetic and semiconducting properties, $CuFe_2O_4$ and other ferrites have been widely used in the electronics industry [21, 22].

In this work $CuFe_2O_4$–TiO_2–Ag nanocomposites were synthesized by a simple precipitation and hydrothermal method. The photo catalytic behaviour of $CuFe_2O_4$–TiO_2–Ag and TiO_2–Ag nanocomposites were evaluated using the degradation of three various azo dyes under ultraviolet and visible lights irradiation. The results show that our synthesized nanocomposites have superparamagnetic behaviours and are applicable for photo-catalytic performance.

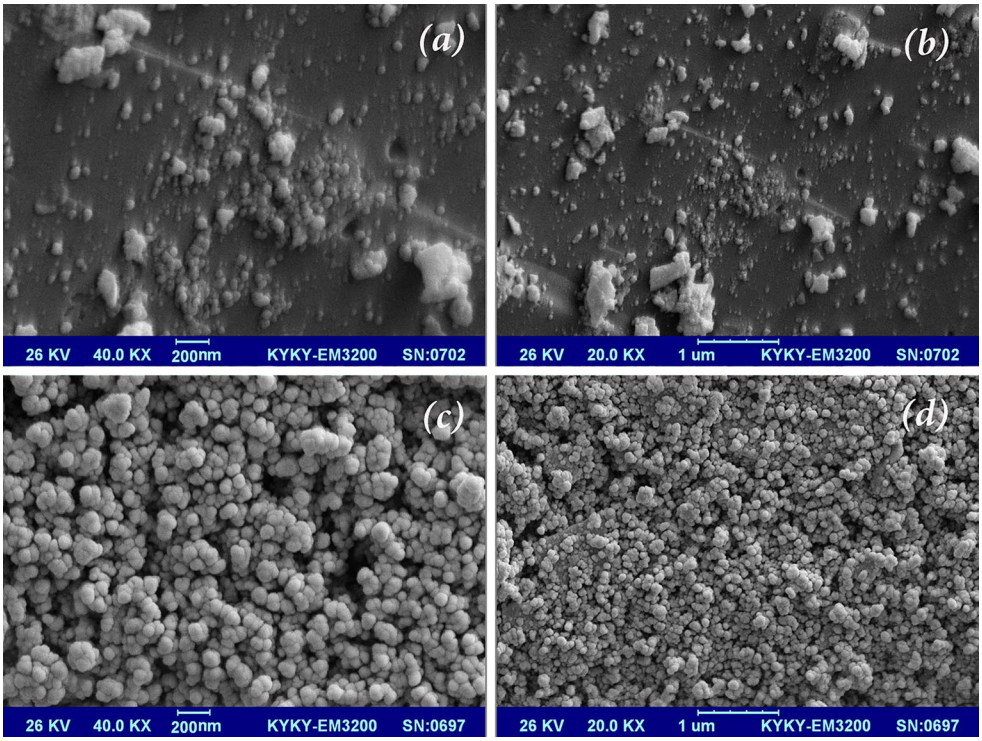

Fig. 5 SEM images of $CuFe_2O_4$–TiO_2 nanocomposite **a**, **b** 2:1, **c**, **d** 1:1

2 Experimental

2.1 Materials and methods

$Fe(NO_3)_3{\cdot}9H_2O$, $Cu(NO_3)_2{\cdot}3H_2O$, NaOH, $AgNO_3$, lactose, glucose, starch, sucrose, $NaBH_4$, distilled water, titanium tetra-isopropoxide (TTIP) were purchased from Merck Company, methanol, acetic acid and nitric acid (HNO_3). XRD patterns were recorded by a Philips, X-ray diffractometer using Ni-filtered CuK_α radiation. SEM images were obtained using a LEO instrument model 1455VP. All the chemicals were used as received without further purifications. Room temperature magnetic properties were investigated using an alternating gradient force magnetometer (AGFM and VSM) device, (Meghnatis Kavir Kashan Co., Iran) in an applied magnetic field sweeping between ±10000 Oe. Prior to taking SEM images, the samples were coated by a very thin layer of Pt (using a BAL-TEC SCD 005 sputter coater) to make the sample surface conductor and prevent charge accumulation, and obtaining a better contrast. A multiwave ultrasonic generator (Bandeline MS 73), equipped with a converter/transducer and titanium oscillator, operating at 20 kHz with a maximum power output of 150 W was used for the ultrasonic irradiation.

2.2 Synthesis of $CuFe_2O_4$ nanoparticles

Firstly 0.64 g of $Fe(NO_3)_3{\cdot}9H_2O$ and 0.2 g of $Cu(NO_3)_2{\cdot}3H_2O$ were dissolved in 100 ml of distilled water. Then NaOH solution (1 M) was slowly added to the solution under microwave radiation (170, 680 and 850 W) for 5 min (30 s on, 30 s off). The pH of the solution was adjusted to 10. The obtained brown precipitate is then centrifuged and was washed twice with distilled water. The product was dried in oven for 24 h and followed by calcination at 200 °C for 2 h.

2.3 Synthesis of silver nanoparticles

0.1 g of $AgNO_3$ was dissolved in 100 ml of distilled water. 0.1 g of lactose (glucose, starch and sucrose) was then added to the solution as surfactant. Then 0.5 g of $NaBH_4$ was dissolved in 10 ml of distilled water. After that, 1 ml of $NaBH_4$ solution was slowly added to the above solution while it was stirred for 15 min. Dark green solution was observed upon addition of $NaBH_4$ (light green solution was observed for starch and sucrose). After 10 min, silver precipitate was observed. The precipitate was collected by centrifugation and was washed with distilled water and it was dried at room temperature.

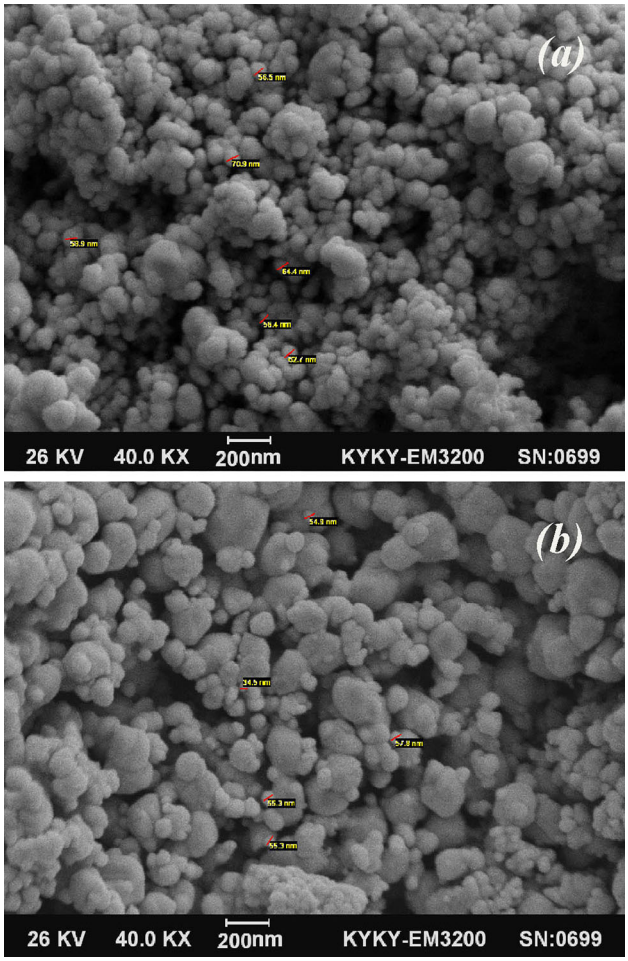

Fig. 6 SEM images of Ag nanoparticles surfactant free prepared by **a** 1 ml of $NaBH_4$, **b** 3 ml of $NaBH_4$

2.4 Synthesis of $CuFe_2O_4$–TiO_2 nanocomposites with a ratio of 2:1 ($CuFe_2O_4$:TiO_2)

Firstly 0.08 g of synthesized copper ferrite (680 W) was dispersed in 10 ml of methanol. It was mixed on magnetic stirring for 15 min. Then 0.1 g of titanium tetra-isopropoxide (TTIP) was added to the solution and was mixed for 10 min. After that 0.6 ml of distilled water was added and the solution was stirred for 10 min. HNO_3 was slowly added to the solution until pH reaches to 1.8. After 60 min stirring the gel was obtained. Then it was dried in oven for 45 min and was calcinated at 500 °C for 2 h.

2.5 Synthesis of $CuFe_2O_4$–TiO_2–Ag nanocomposites

0.1 g of synthesized $CuFe_2O_4$–TiO_2 was dispersed in 100 ml of distilled water. The solution was stirred for 30 min. Then 0.2 g of $AgNO_3$ was added and the solution was stirred for 15 min. Afterwards 1 ml of $NaBH_4$ solution was slowly added to the above mentioned solution and it was stirred for 15 min. The resulting product was collected by centrifugation, washed with distilled water and then dried at room temperature. The schematic diagram of the preparation methods used in this work is presented in Fig. 1.

2.6 Synthesis of $CuFe_2O_4$–TiO_2–Ag nanocomposites by hydrothermal method

1 g of acetic acid was slowly added to the 5 g of titanium tetra isopropoxide (TTIP) and solution was stirred for 15 min (solution 1). Then 0.3 g of synthesized $CuFe_2O_4$ (680 W) was dispersed in 50 ml of distilled water by ultrasonic for 10 min (solution 2). After that, 0.2 g of $AgNO_3$ was added and the solution 2 was stirred for 20 min (solution 3). In the next step, the solution 1 was slowly added to the solution 3 and was stirred for 1 h. HNO_3 was added to the solution (pH reaches to 1.5). The solution is poured in a closed bottle and put in a water bath. Then, the temperature of solution at 75 °C for 45 min was kept. After the solution was cooled, it was treated with an ultrasonic instrument for 20 min and was put in an autoclave and heated at 220 °C for 12 h. The solution was remained at room temperature for 5 h, 0.6 ml HNO_3 added to the solution and it was treated with an ultrasonic instrument for 20 min. In the last step, the precipitate was collected by centrifugation and was washed with distilled water and ethanol and it was dried in oven at 75 °C for 24 h.

2.7 Photo-catalytic degradation process

10 ml of the dye solution (20 ppm) was used as a model pollutant to determine the photocatalytic activity. 0.1 g of catalyst was applied for degradation of 10 ml solution. The solution was mixed by a magnet stirrer for 1 h in darkness to determine the adsorption of the dye by catalyst and better availability of the surface. The solution was irradiated by a 10 W UV lamp which was placed in a quartz pipe in the middle of reactor. It was turned on after 1 h stirring the solution and sampling (about 10 ml) was done every 15 min. After the test photocatalysts, the solution was placed in visible light for 1 h. The samples were filtered, centrifuged and their concentration was determined by UV–visible spectrometry.

3 Results and discussion

The XRD shows that silver synthesis nanoparticles are crystalline (Fig. 2a). The size of the Ag nanoparticles estimated from the Scherrer formula is about 30 nm. A

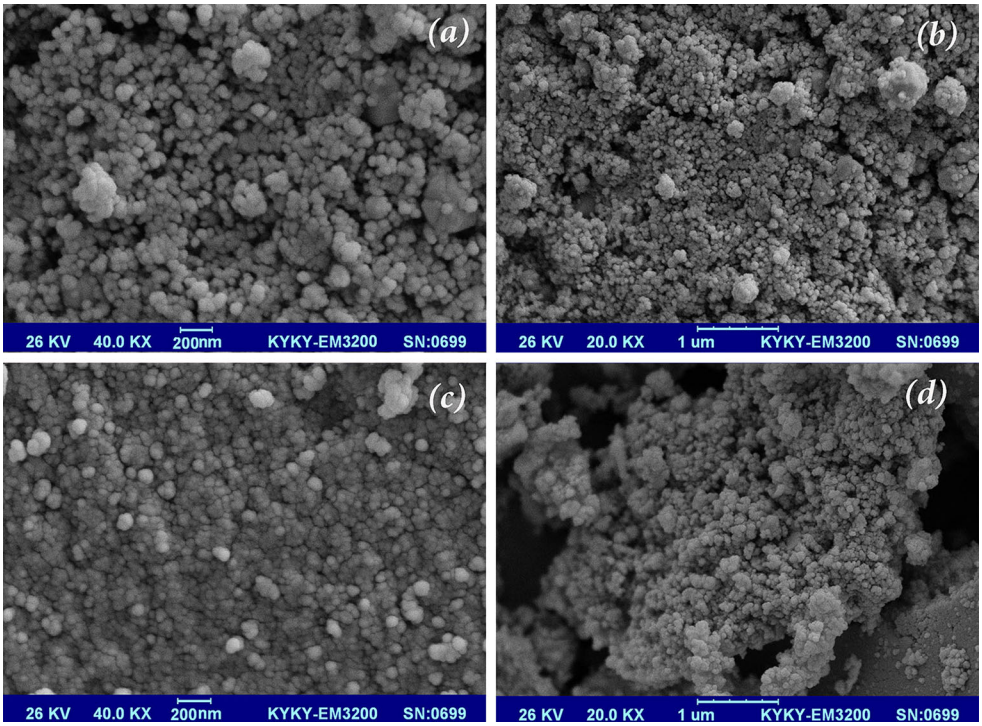

Fig. 7 SEM images of silver nanoparticle obtained by **a**, **b** lactose, **c**, **d** glucose

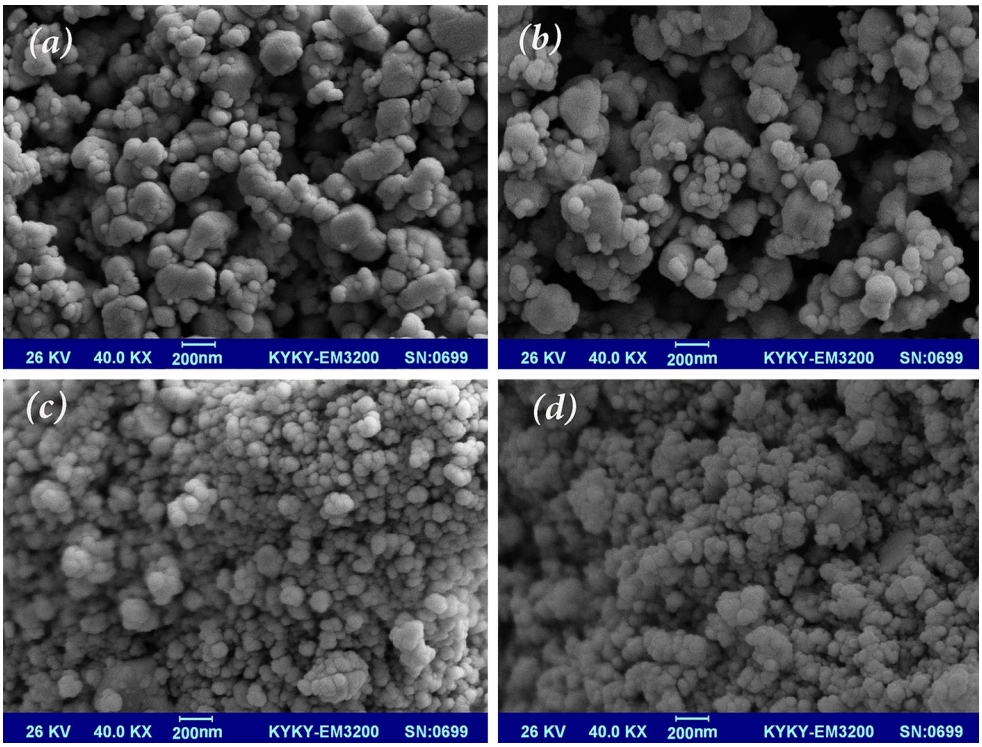

Fig. 8 SEM images of silver nanoparticle prepared by **a**, **b** sucrose, **c**, **d** starch

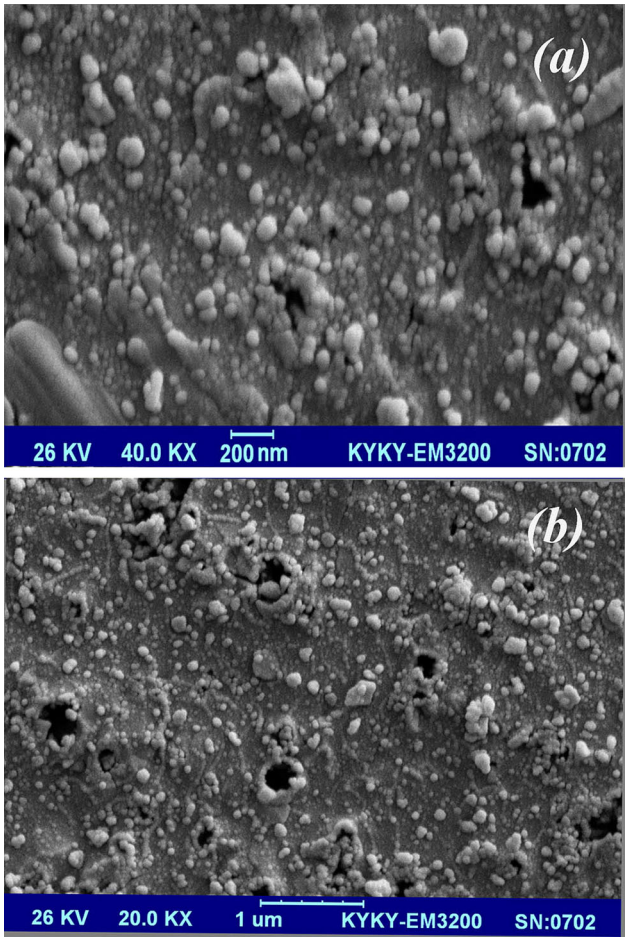

Fig. 9 SEM images of TiO_2–Ag nanocomposite

number of strong Bragg reflection peaks can be seen which correspond to the (111), (200), (220) and (311) reflections of FCC silver and lattice parameters of $a = b = c = 4.070$ Å. The standards (JCPDS), silver file No. 04-0783 and space group of Fm-3m (space group number: 225) in the pattern are reported [23].

Figure 2b shows XRD pattern of TiO_2 nanoparticle product. It can be observed that Anatase phase with (JCPDS No. 21-1272) and space group of I41/amd is presented in the pattern.

The composition of the TiO_2–Ag nanocomposite was investigated by XRD pattern and it is depicted in Fig. 2c. It confirms presence of both phase of Ag (JCPDS No. 04-0783) and Anatase phase of TiO_2 (JCPDS No. 21-1272) in the pattern. The peak intensities related to each counterpart are relatively similar, which is representative of rather equal portion of the shared compounds in the composite. The crystalline sizes are calculated from Scherrer equation, $D_c = K\lambda/\beta Cos\theta$, where β is the width of the observed diffraction peak at its half maximum intensity (FWHM), K is the shape factor, which takes a value of about 0.9, and λ is the X-ray wavelength (CuK_α radiation, equals to 0.154 nm). The values of about 15 and 13 nm were found for crystalline sizes of $CuFe_2O_4$–TiO_2 and $CuFe_2O_4$–TiO_2–Ag nanocomposites, respectively.

Figure 3a illustrates XRD pattern of $CuFe_2O_4$–TiO_2 product. Cubic phase of copper ferrite with JCPDS No. 25-0283 (space group of Fd-3m) and Anatase phase for TiO_2 with (JCPDS No. 21-1272) and space group of I41/amd can be observed in this pattern. XRD pattern of $CuFe_2O_4$–TiO_2–Ag nanocomposites is shown in Fig. 3b. Presence of three phases of copper ferrite, titanium dioxide and silver was confirmed by XRD pattern.

The SEM images of the magnetic $CuFe_2O_4$ nanoparticles at different power of microwave radiation are presented in Fig. 4. Figure 4a, b illustrate SEM image (in two different magnifications) of as-synthesized $CuFe_2O_4$ nanoparticles with a power of 170 W. The images indicate that nanoparticles with average diameter size of less than 70 nm were prepared. The agglomeration of particles in power 170 W was observed. Figure 4c, d illustrate SEM image (in two magnifications) of the $CuFe_2O_4$ nanoparticles obtained at 680 W and show nanoparticles with mediocre diameter size of about 60 nm. The SEM image of $CuFe_2O_4$ nanoparticles by power of 850 W is shown in Fig. 4e, f. According to SEM image with increase in microwave power smaller size and uniform morphologies was synthesized. One reason could be that because more energy at high power, nucleation stage is preferential compare to growth stage.

SEM images of $CuFe_2O_4$–TiO_2 nanocomposite are shown in Fig. 5. In Fig. 5a, b, the nanocomposite was synthesized with a ratio of 2:1. Figure 5c, d illustrate SEM image (in two different magnifications) of as-synthesized $CuFe_2O_4$–TiO_2 nanocomposite with a ratio of 1:1. According to the SEM images, can be seen smaller nanocomposites were synthesized and ratio of 1:1 shows more uniform morphology in comparison to ratio of 2:1. The particle density is more regular too. Figure 6a shows SEM images of the silver nanoparticles by 1 ml of $NaBH_4$ solution. Figure 6b illustrate SEM image of the Ag nanoparticles obtained with 3 ml of reducing agent. It seems by using higher amounts of $NaBH_4$ (3 ml), show larger particles.

Effect of various sugars as green, bio-degradable and cost-effective capping agent on the morphology and particle size of silver nanoparticles was investigated. Figure 7a, b exhibit SEM images of Ag which achieved by lactose capping agent. The images show the size of mono-disperse

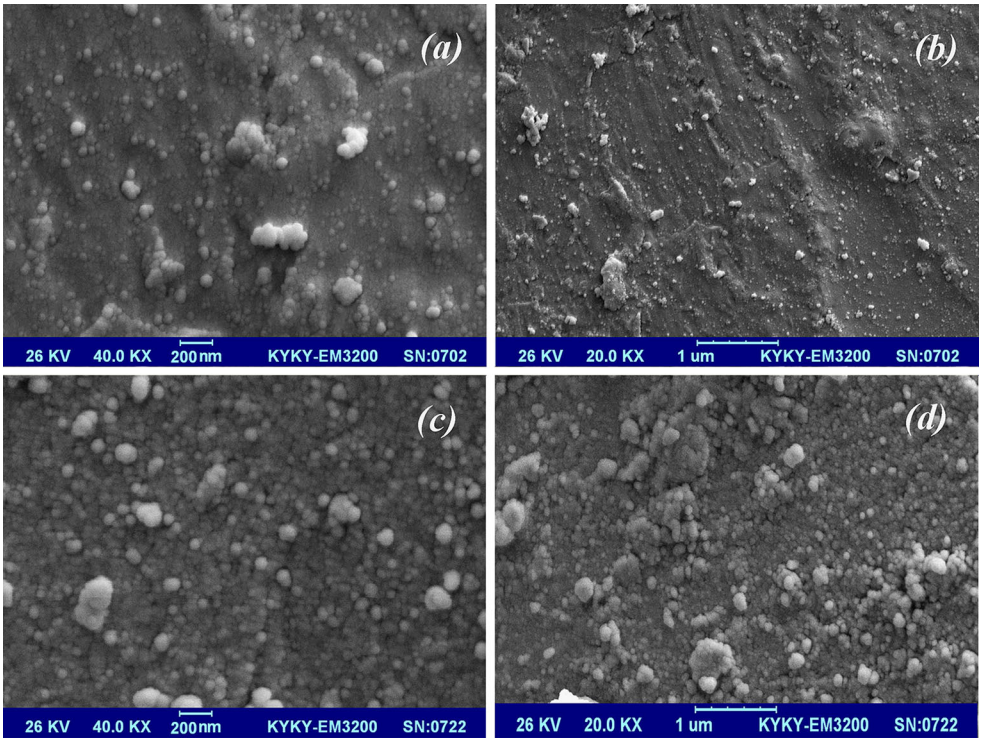

Fig. 10 SEM images of **a**, **b** $CuFe_2O_4$–TiO_2–Ag nanocomposite by precipitation method, **c**, **d** $CuFe_2O_4$–TiO_2–Ag nanocomposite by hydrothermal method

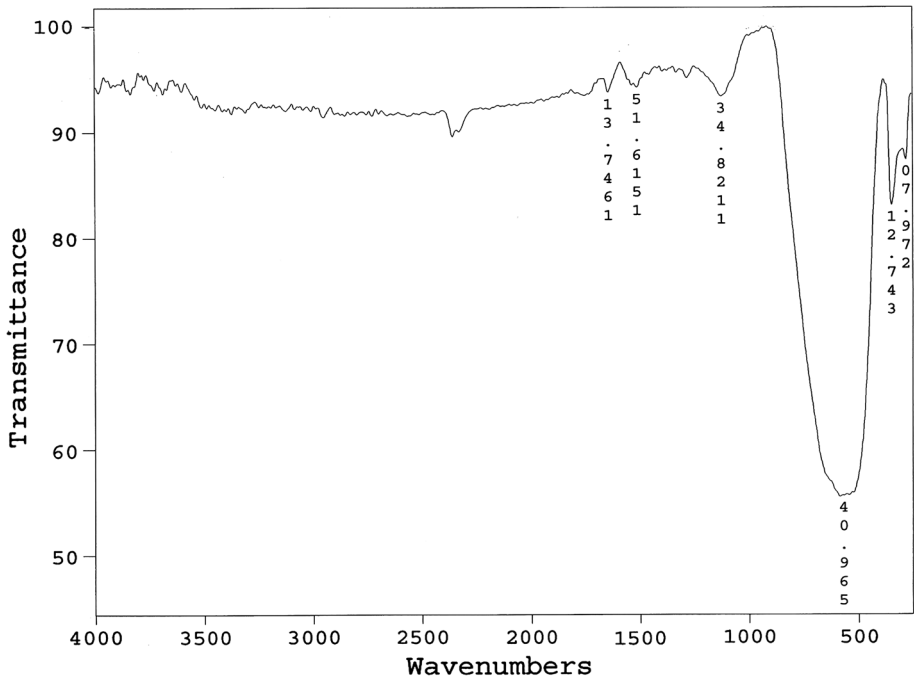

Fig. 11 FT-IR spectrum of TiO_2 nanoparticles

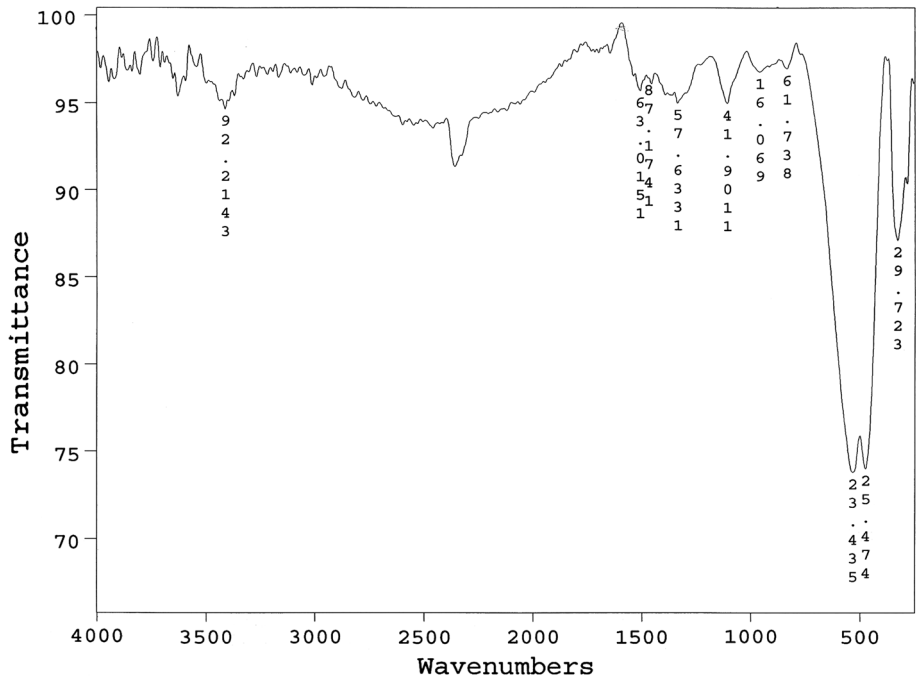

Fig. 12 FT-IR spectrum of $CuFe_2O_4$–TiO_2 nanocomposite

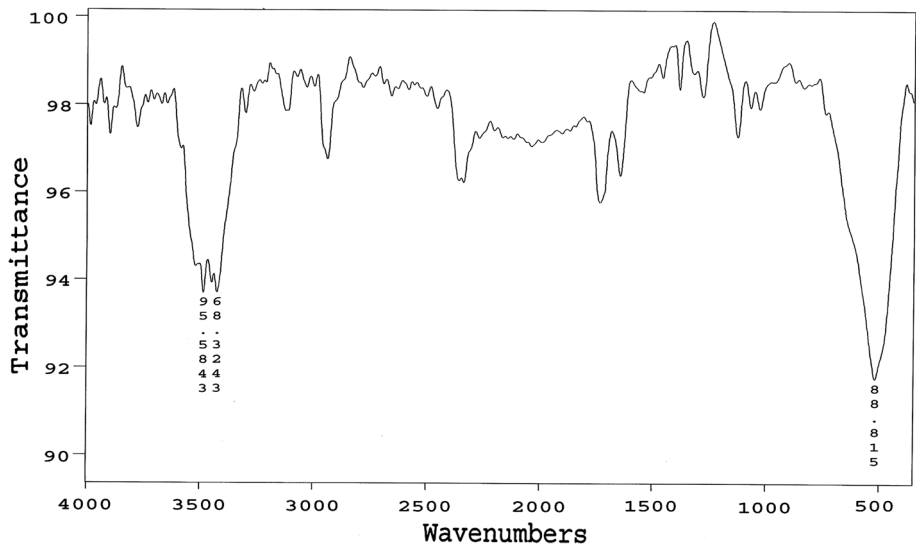

Fig. 13 FT-IR spectrum of TiO_2–Ag nanocomposite

particles is about 40 nm. Figure 7c, d shows SEM images of the product achieved by glucose and approve particles are mono-disperse with average size of about 50 nm.

SEM images of the silver obtained by sucrose are illustrated in Fig. 8a, b and approve preparation of nanoparticles with average size of around 70 nm. Using sucrose as surfactants larger sizes of the particles were synthesized. Figure 8c, d depict SEM images of the obtained silver by starch. The images show the size of particles is around 50–60 nm. Among surfactants that were used, it seems lactose is the most effective surfactant for preparation of smaller nanoparticles.

SEM images of TiO_2–Ag nanocomposite are shown in Fig. 9a, b and approve preparation of nanoparticles with average size of 30–40 nm. Figure 10a, b illustrate SEM images in two different magnifications of as-synthesized $CuFe_2O_4$–TiO_2–Ag nanocomposites by precipitation method.

Figure 10c, d illustrate SEM image in two different magnifications of as-synthesized $CuFe_2O_4$–TiO_2–Ag

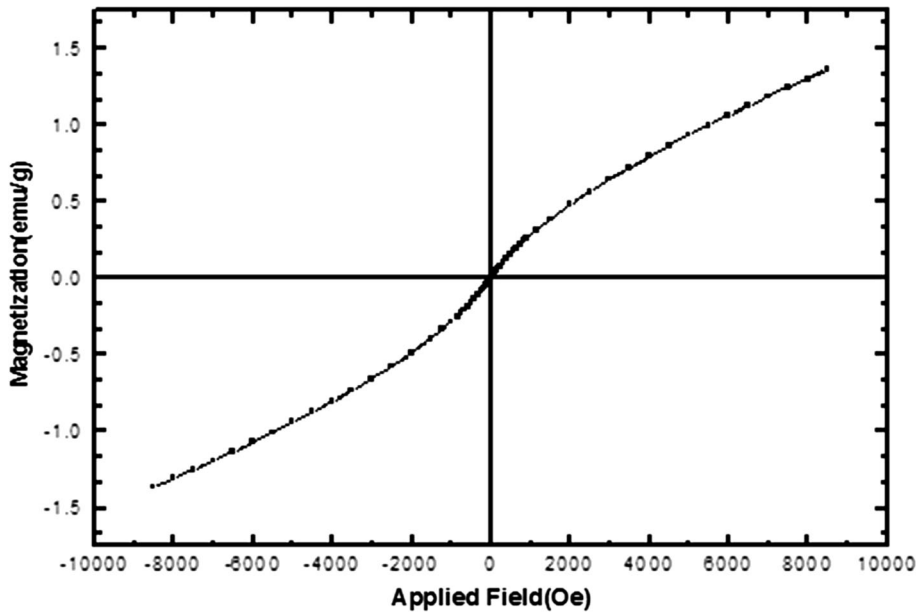

Fig. 14 Room temperature magnetization curve of $CuFe_2O_4$ nanoparticles (200 °C)

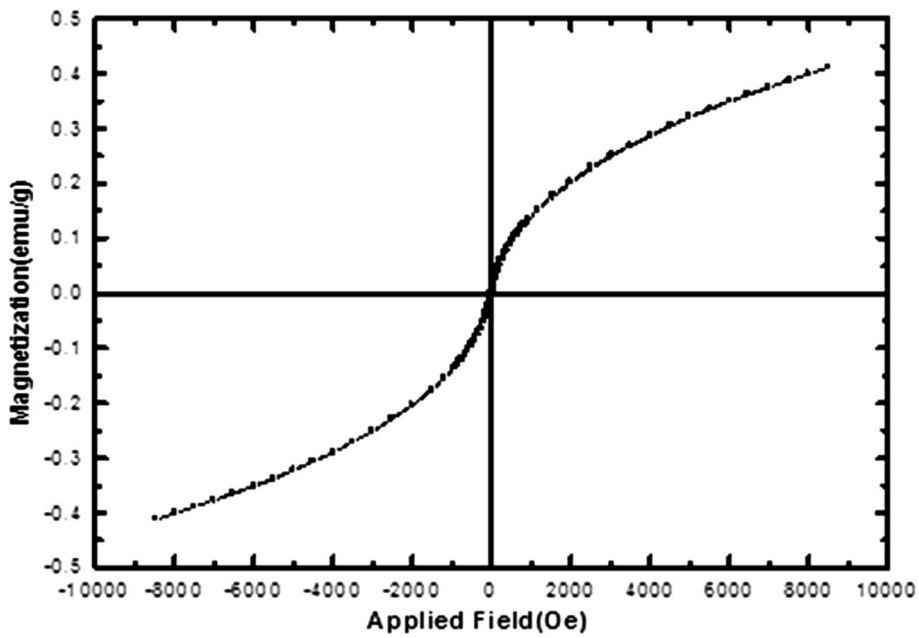

Fig. 15 Room temperature magnetization curve of $CuFe_2O_4$–TiO_2 nanocomposite (2:1)

nanocomposites by hydrothermal method. The images approve formation of mono-disperse structures with average particle size of around 30 nm.

Figure 11 illustrates the FT-IR spectrum of the as-prepared titanium dioxide. The absorption band at 569 cm^{-1} is assigned to the Ti–O bonds. Figure 12 shows the FT-IR spectrum of the as-prepared $CuFe_2O_4$–TiO_2 nanocomposites. The absorption band at 534 cm^{-1} is assigned to the Ti–O vibration, absorption band at 474 cm^{-1} is assigned to the Cu–O (metal–oxygen bonds) and absorption band at 327 cm^{-1} is assigned to the Fe–O bonds. Figure 13 illustrates the FT-IR spectrum of the as-prepared TiO_2–Ag nanocomposite. The broad absorption peaks at 3485 and 3423 cm^{-1} which are assigned to adsorbed O–H groups on the surface of nanoparticles. The absorption band at 518 cm^{-1} is assigned to the Ti–O bond. There are no other significant peaks related to precursors and other impurities.

Room temperature magnetic properties of samples were studied using an AGFM instrument. Magnetization curve for $CuFe_2O_4$ nanoparticles is shown in Fig. 14. The curve

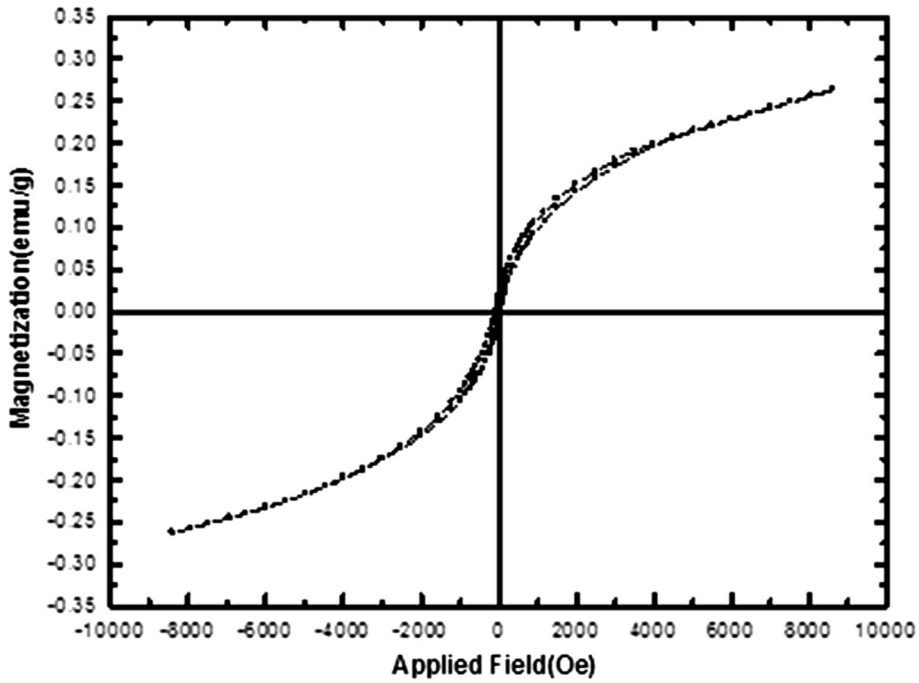

Fig. 16 Room temperature magnetization loop of $CuFe_2O_4$–TiO_2–Ag nanocomposite

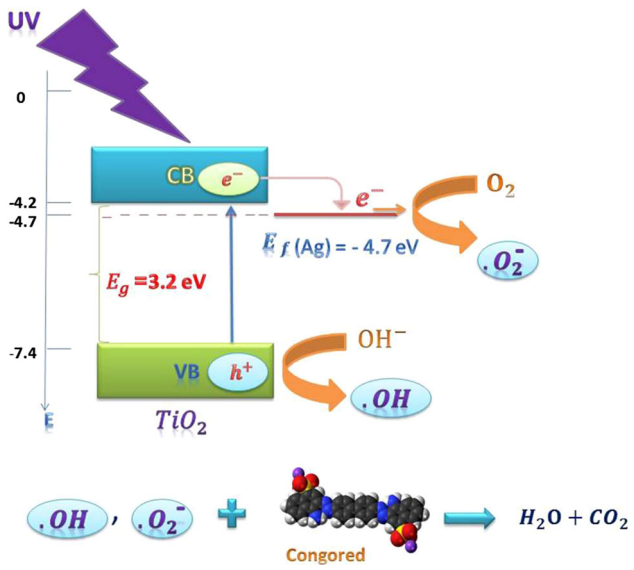

Fig. 17 Schematic of the mechanism photocatalytic properties of TiO_2–Ag nanocomposite under UV light

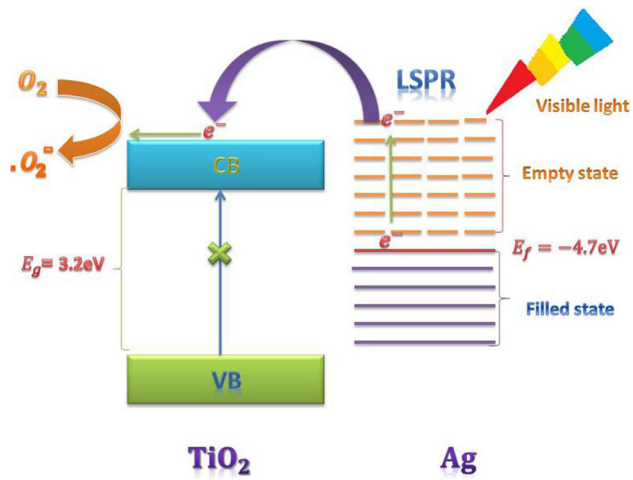

Fig. 18 Schematic of the mechanism photocatalytic properties of TiO_2–Ag nanocomposite under visible light

indicates that the synthesized ferrite nanoparticles which annealed at 200 °C exhibits superparamagnetic behaviour with a zero coercivity and a magnetization of 1.5 emu/g when subjected to an applied magnetic field of 8000 Oe. Magnetization curve of magnetic $CuFe_2O_4$–TiO_2 nanocomposites is shown in Fig. 15. The curve indicates that this sample also exhibit show superparamagnetic behaviour with a magnetization of 0.42 emu/g. The magnetic property of prepared $CuFe_2O_4$–TiO_2–Ag nanocomposite was also investigated. The result shows superparamagnetic behaviour with a saturation magnetization of 0.28 emu/g and a coercivity of 50 Oe in Fig. 16. This sample has sufficient magnetizations which can simply be attracted by a laboratory magnet, making them appropriate for core of recyclable photocatalyst. This magnetization indicates that $CuFe_2O_4$–TiO_2 and $CuFe_2O_4$–TiO_2–Ag nanocomposites inherit the magnetic property

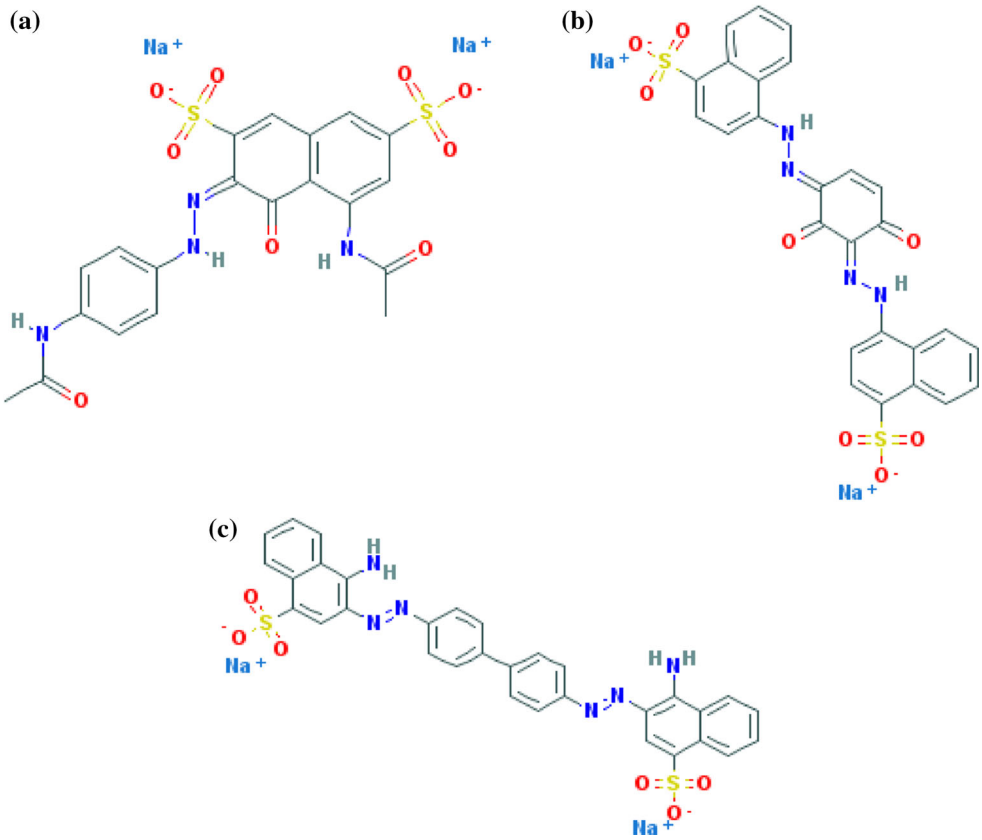

Fig. 19 Chemical formulas of azo dyes, **a** acid violet, **b** acid brown 14, **c** Congored

from the $CuFe_2O_4$. However, the magnetizations are lower due to presence of titanium dioxide and silver. This reduction in saturation magnetization is due to the interfacial effect of the typical nanocomposite. The magnetic property of the prepared nanocomposites is an essential characteristic of a re-generable and re-usable magnetic heterogeneous catalyst.

Schematics of the photocatalytic mechanism of TiO_2–Ag nanocomposite under UV light and visible light are shown in Figs. 17 and 18 respectively. In photocatalytic activity of Ag–TiO_2 under UV light, presence of silver nanoparticle in Ag–TiO_2 nanocomposites acts as an electron trap and prevents the electron hole recombination, which is important factor in determining the photocatalytic activity as represented in Fig. 17. The collision visible light to the nanocomposite, localized surface plasmon resonance (LSPR) occurs on silver nanoparticles. If the electron from the filled state of silver nanoparticles (Levels below the Fermi level), to be excited to levels above the conduction band of TiO_2 nanoparticle (due to desire of electrons to be at the lower energy level) transferred to the conduction band of TiO_2. Then the electrons reduce oxygen molecules and produce super oxide anion that able to decompose toxic organic contaminants Fig. 18 [23–27].

Chemical formulas of azo dyes acid violet, acid brown 14 and Congored are shown in Fig. 19. The photo-catalytic activity of the $CuFe_2O_4$–TiO_2–Ag and TiO_2–Ag nanocomposites was evaluated by monitoring the degradation of three azo dyes in an aqueous solution, under irradiation of UV light and visible light. The changes in the concentration of dye at presence of TiO_2–Ag nanocomposites are illustrated in Figs. 20 and 21. The photo-degradation of Congored, acid brown and acid violet at presence of $CuFe_2O_4$–TiO_2–Ag nanocomposites are illustrated in Figs. 22, 23 and 24 respectively. Three component nanocomposites show better outcome in comparison to the

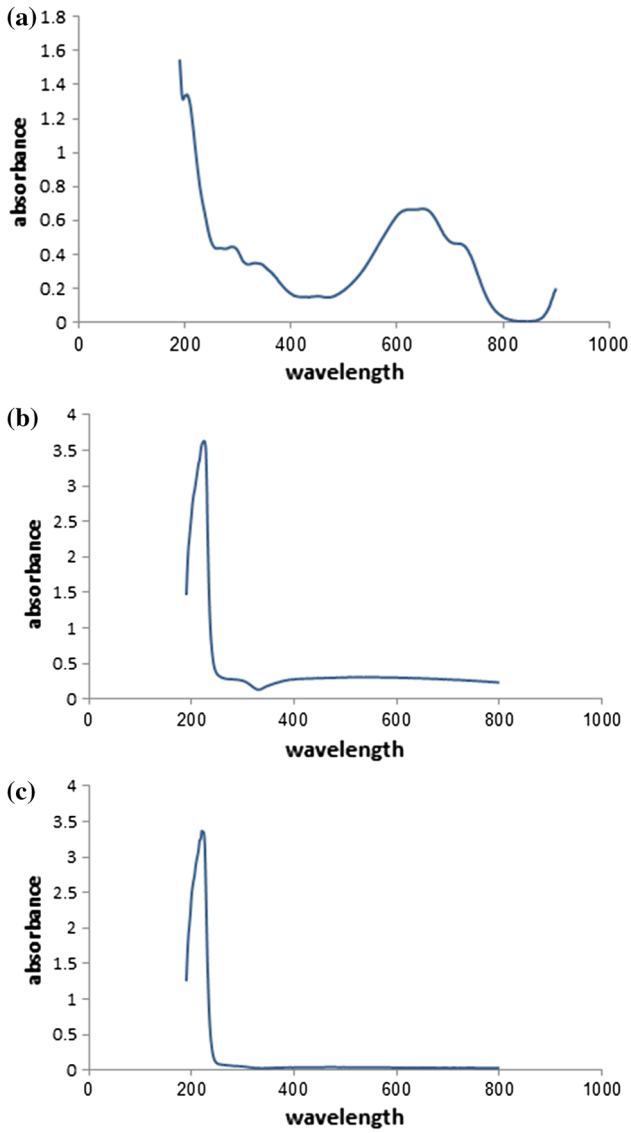

Fig. 20 UV–Vis spectra of TiO_2–Ag nanocomposite of degradation of Congored **a** 0 min, **b** 60 min under UV light, **c** visible light

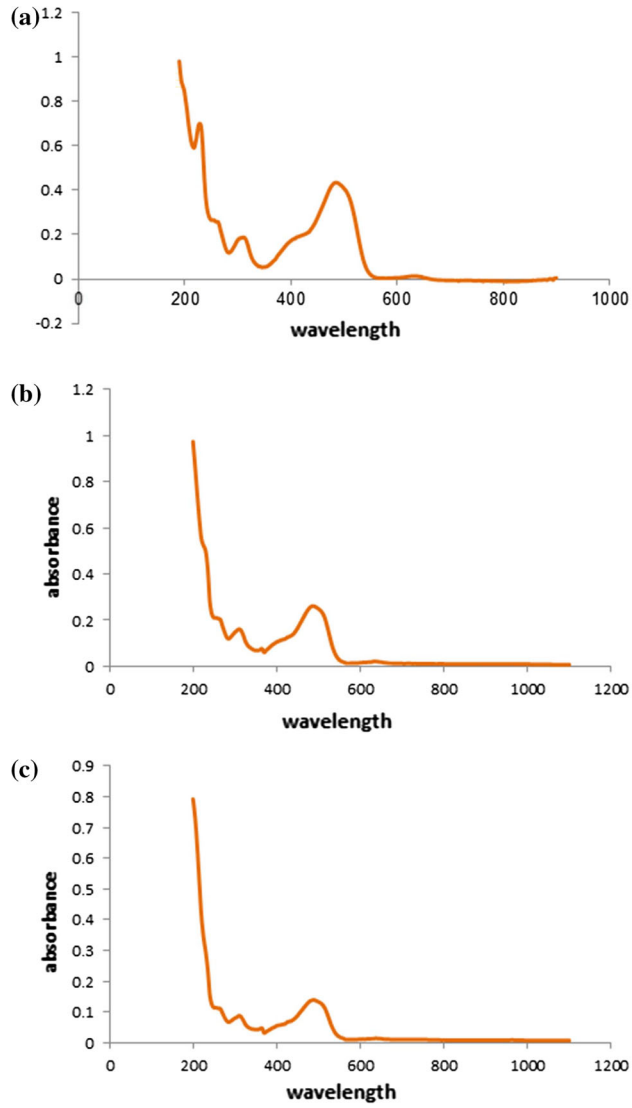

Fig. 21 UV–Vis spectra of TiO_2–Ag nanocomposite of degradation of acid brown 14 **a** 0 min, **b** 60 min under UV light, **b** visible light

two components TiO_2–Ag product. Acid violet, acid brown 14 and Congored were degraded for $CuFe_2O_4$–TiO_2–Ag nanocomposites around 70, 80 and 90 % at 60 min respectively under ultra violet light. Interestingly results confirm that azo-dyes degradation under visible light are higher and faster comparing to ultraviolet radiation. Acid violet, acid brown 14 and Congored were degraded for $CuFe_2O_4$–TiO_2–Ag nanocomposites around 95, 80 and

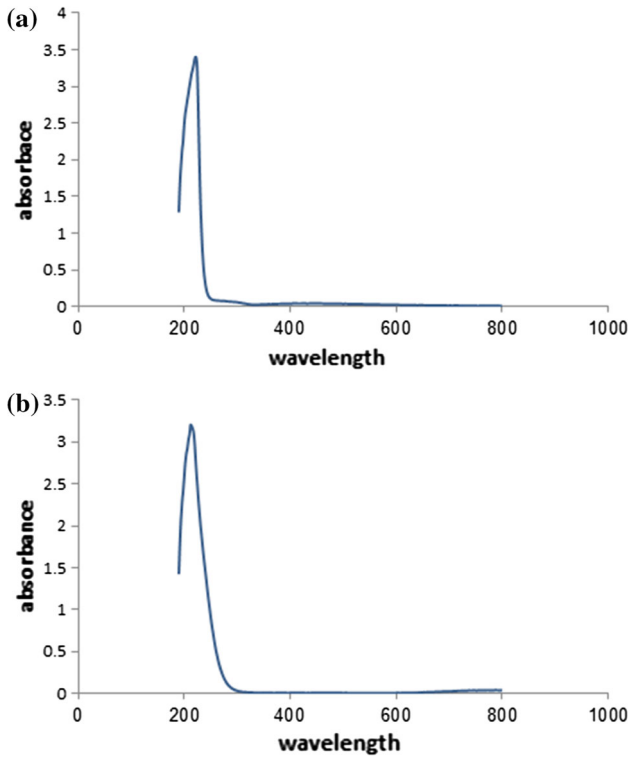

Fig. 22 UV–Vis spectra of $CuFe_2O_4$–TiO_2–Ag nanocomposite of degradation of Congored **a** 60 min under UV light, **b** visible light

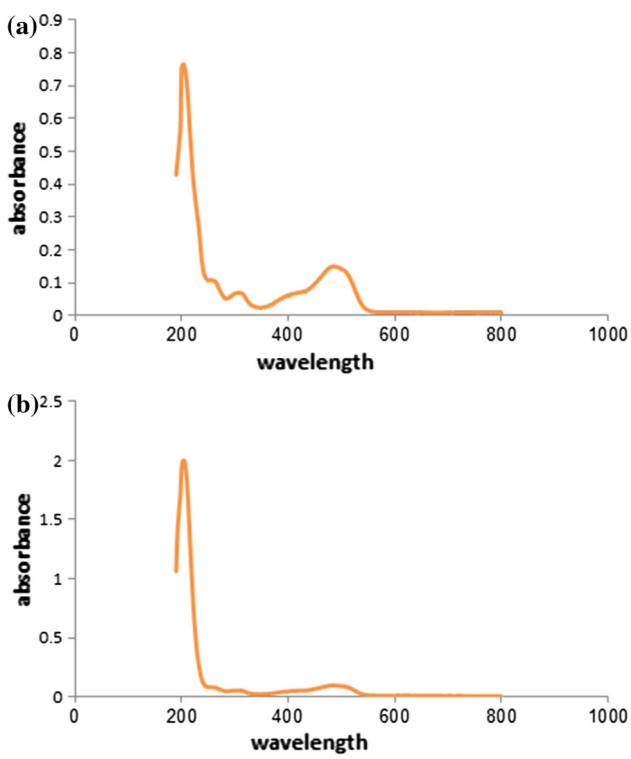

Fig. 23 UV–Vis spectra of $CuFe_2O_4$–TiO_2–Ag nanocomposite of degradation of acid brown 14 **a** 60 min under UV light, **b** visible light

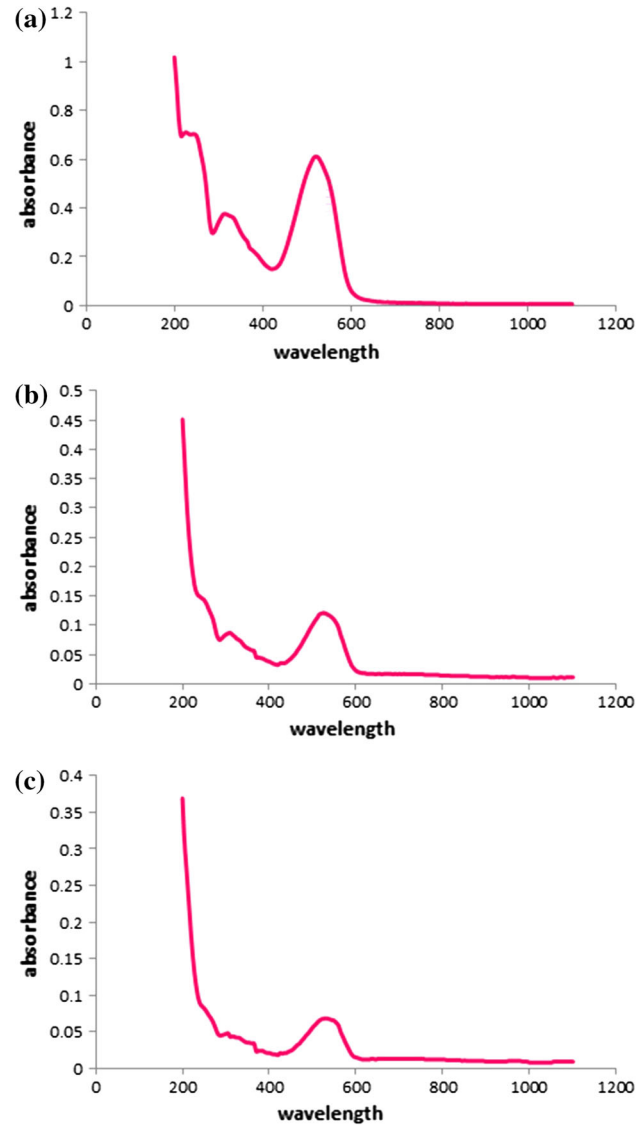

Fig. 24 UV–Vis spectra of $CuFe_2O_4$–TiO_2–Ag nanocomposite of degradation of acid violet **a** 0 min, **b** 60 min under UV light, **c** visible light

99 % at 60 min respectively under visible light. Organic dyes decompose to water, carbon dioxide and other less toxic or nontoxic residuals [24, 25, 28]. These nanocomposites introduce an applicable photocatalyst for industrial water purification from toxic pollutants. Figure 25 shows photo-degradation of three azo dyes after 60 min exposure to visible light at presence of $CuFe_2O_4$–TiO_2–Ag nanocomposite. The differences between $CuFe_2O_4$–TiO_2 [28] and $CuFe_2O_4$–TiO_2–Ag nanocomposites are shown in Table 1.

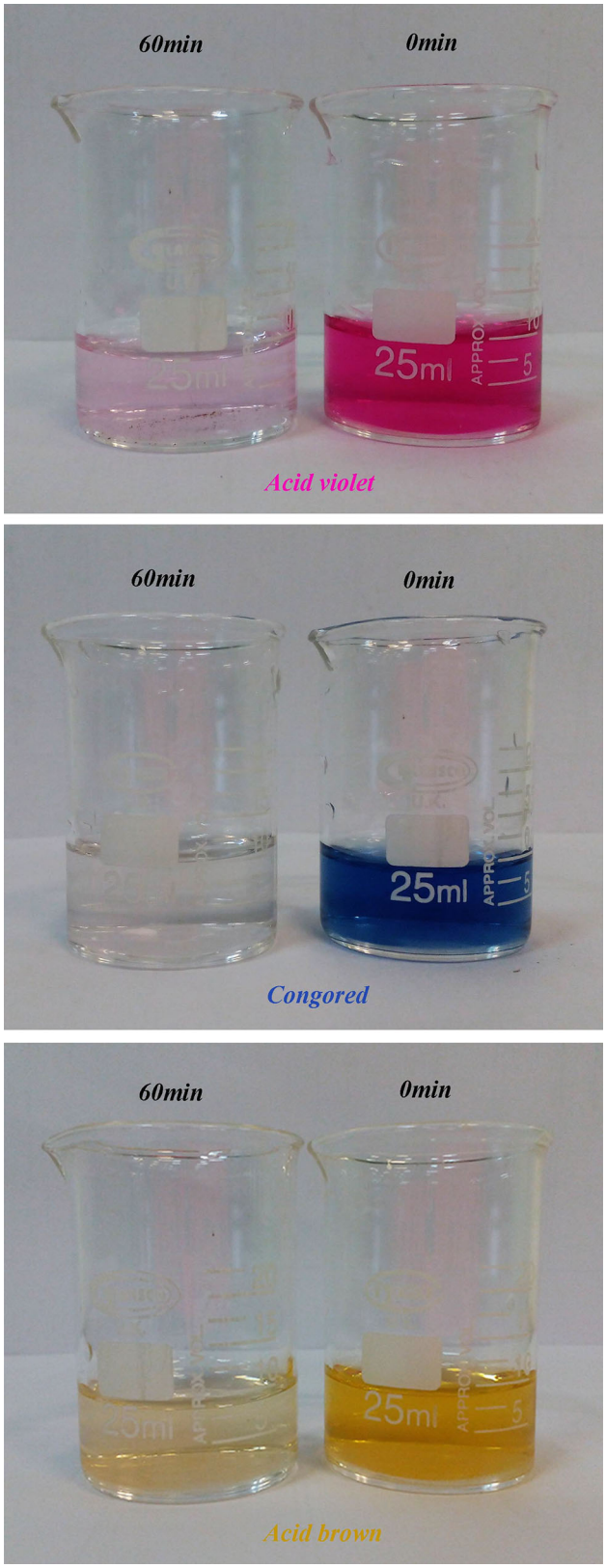

Fig. 25 Photocatalytic activity of $CuFe_2O_4$–TiO_2–Ag nanocomposite under visible light

Table 1 Differences between $CuFe_2O_4$–TiO_2 and $CuFe_2O_4$–TiO_2–Ag

Differences	Previous work Two components [28]	Present work Three components
Preparation of $CuFe_2O_4$	Precipitation	Microwave
Preparation of TiO_2	Sol–gel	Sol–gel, hydrothermal
Ratio of $CuFe_2O_4$–TiO_2	1:1	1:1 and 2:1
Ag phase	No	Yes
Surfactant ($CuFe_2O_4$)	Yes	No
Temperature ($CuFe_2O_4$)	200–600 °C	200 °C
Temperature (TiO_2)	500 °C	Hydrothermal 220 °C
Photocatalytic	UV	UV and visible
Organic dyes	Black, blue, brown, congo	Violet, brown, congo

4 Conclusions

Firstly copper ferrite nanoparticles were synthesized then $CuFe_2O_4$–TiO_2–Ag nanocomposites were prepared via a simple precipitation method and hydrothermal method. Effects of various surfactants on the morphology and particle size of the silver nanoparticles were investigated. Effects of power of microwave on the morphology and particle size of the $CuFe_2O_4$ nanoparticle were also investigated. AGFM confirmed that $CuFe_2O_4$–TiO_2 and $CuFe_2O_4$–TiO_2–Ag nanocomposites exhibit superparamagnetic behaviour. The photocatalytic behaviour of $CuFe_2O_4$–TiO_2–Ag and TiO_2–Ag nanocomposites were evaluated using the degradation of three azo dyes under UV light irradiation and visible light. The results show that precipitation and hydrothermal method are suitable method for preparation of $CuFe_2O_4$–TiO_2–Ag nanocomposites as a candidate for photocatalytic applications.

Acknowledgments This work has been supported financially by Arak University Research Council (AURC) under the Grant Number of 95-148 [95-2-13]. The authors acknowledge AURC for the financial support.

References

1. D. Ding, K. Liu, S. He, C. Gao, Y. Yin, J. Nano Lett. **14**, 6731–6736 (2014)
2. M. Tariq Qamar, M. Aslam, I.M.I. Ismail, N. Salah, A. Hameed, ACS Appl. Mater. Interfaces **7**, 8757–8769 (2015)
3. T. Takata, C. Pan, M. Nakabayashi, N. Shibata, K. Domen, J. Am. Chem. Soc. doi:10.1021/jacs.5b04107

4. L.S. Daniel, H. Nagai, N. Yoshida, M. Sato, Catalysts **3**, 625–645 (2013)
5. M.J. Kale, T. Avanesian, P. Christopher, ACS Catal. **4**, 116–128 (2014)
6. C.L. Muhich, J.Y. Westcott, T. Fuerst, A.W. Weimer, C.B. Musgrave, J. Phys. Chem. C **118**, 27415–27427 (2014)
7. Z. Peng, H. Tang, Y. Tang, K.F. Yao, H.H. Shao, Int. J. Photo (2014); Article ID 867565
8. P. Wang, B. Huang, Y. Daia, M.-H. Whangbo, Chem. Phys. **14**, 9813–9825 (2012)
9. W.J. Tseng, S.-M. KaoA, J.H. Hsieh, J. Ceram. Int. **04**, 139 (2015)
10. Z. Liu, W. Hou, P. Pavaskar, M. Aykol, S.B. Cronin, J. Nano Lett. **11**, 1111–1116 (2011)
11. G. Baffoua, R. Quidant, Chem. Soc. Rev. **43**, 3898–3907 (2014)
12. P. Christopher, D.B. Ingram, S. Linic, J. Phys. Chem. C **114**, 9173–9177 (2010)
13. X. Wang, T. Wu, H. Wang, X. Su, Mater. Res. Bull. **73**, 423–428 (2016)
14. R. Liu, P. Wang, X. Wang, H. Yu, J. Yu, J. Phys. Chem. C **116**, 17721–17728 (2012)
15. D. Ghanbari, S. Sharifi, A. Naraghi, G. Nabiyouni, J. Mater. Sci.: Mater. Electron. **27**, 5315–5323 (2016)
16. Y. Yu, P. Zhang, L. Guo, Z. Chen, Q. Wu, Y. Ding, W. Zheng, Y. Cao, J. Phys. Chem. C **118**, 12727–12733 (2014)
17. S.G. Kumar, L.G. Devi, J. Phys. Chem. A **115**, 13211–13241 (2011)
18. M.S.A.S. Shah, A.R. Park, K. Zhang, J.H. Park, P.J. Yoo, A.C.S. Appl, Mater. Interfaces **4**, 3893–3901 (2012)
19. D. Tsukamoto, Y. Shiraishi, Y. Sugano, S. Ichikawa, S. Tanaka, T. Hirai, J. Am. Chem. Soc. **134**, 6309–6315 (2012)
20. A. Allafchian, S.A.H. Jalali, H. Bahramian, H. Ahmadvand, J. Magn. Magn. Mater. **404**, 15–20 (2015)
21. C. Munteanu, M. Caldararu, D. Gingasu, M. Feder, L. Diamandescu, N.I. Ionescu, React. Kinet. Mech. Catal. **104**, 357 (2011)
22. W. Ponhan, S. Maensiri, Solid State Sci. **11**, 479–484 (2009)
23. M.A. Majeed Khan, S. Kumar, M. Ahamed, S.A. Alrokayan, M.S. AlSalhi, Nanoscale Res. Lett. **6**, 434 (2011)
24. A. Esmaeili-Bafghi-Karimabad, D. Ghanbari, M. Salavati-Niasari, L. Nejati-Moghadam, S. Gholamrezaei, J. Mater. Sci.: Mater. Electron. **26**, 6970–6978 (2015)
25. M. Goudarzi, D. Ghanbari, M. Salavati-Niasari, A. Ahmadi, J. Clust. Sci. (2015). doi:10.1007/s10876-015-0895-5
26. R. Nainani, P. Thakur, M. Chaskar, J. Mater. Sci. Eng. B **2**(1), 52–58 (2012)
27. V. Subramanian, E.E. Wolf, P.V. Kamat, J. Am. Chem. Soc. **126**, 4943–4950 (2004)
28. S. Masoumi, G. Nabiyouni, D. Ghanbari, J. Mater. Sci.: Mater. Electron. (2016). doi:10.1007/s10854-016-5067-3